CrystEngComm

PAPER

View Article Online
View Journal | View Issue

Cite this: *CrystEngComm*, 2015, **17**, 5734

The effect of Se doping on the growth of Te nanorods†‡

Junghyeok Kwak,[a] Chang-Eun Kim,[b] Yuho Min,[b] Ji-Hwan Lee,[b] Aloysius Soon*[b] and Unyong Jeong*[a]

Received 9th December 2014,
Accepted 11th June 2015

DOI: 10.1039/c4ce02431a

www.rsc.org/crystengcomm

In this study, we successfully conducted a series of computationally-assisted experiments, regarding the morphology control and chemical transformation of Te nanorods. The morphology of Te nanorods is controlled by introducing a minute amount of isovalent Se dopant. Density-functional theory calculations predicted the Gibbs surface free energy change due to the adsorbent Se on the major facets of Te nanorods. Encouraged by the theoretical prediction, we conducted experiments on Te nanorod growth and did find significant variation of the morphology of Te nanorods due to Se injection. Furthermore, we demonstrated the chemical transformation of the shape-controlled Te nanorods to binary thermoelectric compounds such as PbTe and Bi_2Te_3 without losing the tailored morphology. The transformed PbTe and Bi_2Te_3 have nanoscale grain boundaries as seen from the cross-section HRTEM image. We emphasize that the robust production of morphology-controlled thermoelectric nanorods can be an optimal approach to develop an advanced thermoelectric composite material, by which the multiscale phonon scattering effect can be maximized.

1. Introduction

Morphology control of nanocrystalline materials is of great interest, as the properties of the nanostructured materials are highly dependent on their dimensions;[1,2] thus, precise control over these dimensions has been greatly sought after. When it comes to syntheses of nanocrystals, solution-based syntheses have notable advantages due to robust yield and uniform properties of the final product. There are several known mechanisms of growing nanocrystals by solution-based methods, including preferential growth of nanocrystal facets,[3,4] surfactant-assisted surface energy control,[5] oriented assembly of multiple nanocrystals,[6] sacrificial templating methods,[7] and chemical transformation of an existing nanocrystal into a completely different compound.[8] Although remarkable advances have been made as reviewed in other reports,[9,10,11] precise control over the geometric dimensions of these materials such as thickness or diameter is yet to be further investigated.

Besides the geometric change of the nanocrystals due to dopants from a fundamental point of view, the shape-controlled Te nanorods can be used to produce an advanced thermoelectric composite. When shape-controlled nanocrystals are used to synthesize a bulk thermoelectric composite, the size and shape of the nanocrystals have a critical impact on the packing factor, porosity, and grain boundary density of the final product. In this aspect, we further conducted chemical transformation of the shape-controlled Te nanorods into functional metal tellurides (M_xTe_y) such as PbTe and Bi_2Te_3.

Metal tellurides (M_xTe_y) are considered promising materials for developing advanced thermoelectric devices.[12] Specifically, Bi_2Te_3, PbTe and their heterostructures have been widely investigated.[13,14] Generally, high electric conductivity, high Seebeck coefficient, and low thermal conductivity are required to improve thermoelectric efficiency. While the electric conductivity and Seebeck coefficient are determined by the electronic structure, the thermal conductivity can be reduced by introducing microstructures such as grain boundaries, line defects or point defects. According to Dresselhaus and Hicks, a remarkable reduction of thermal conductivity can be achieved when nanostructures induce robust phonon scattering phenomenon.[15–17] A straightforward approach to enhance phonon scattering is to increase the proportion of grain boundaries, mainly by using the powder-press method

[a] *Department of Materials Science and Engineering, Pohang University of Science and Technology (POSTECH), San 31, Hyoja-dong, Nam-gu, Pohang, Gyeongbuk 790-784, Republic of Korea. E-mail: ujeong@postech.ac.kr*
[b] *Global E[3] Institute and Department of Materials Science and Engineering, Yonsei University, 50 Yonsei-Ro, Seodaemun-Gu, Seoul 120-749, Republic of Korea. E-mail: aloysius.soon@yonsei.ac.kr*

† The authors declare no competing financial interest.

‡ Electronic supplementary information (ESI) available: Simulation codes and theoretical details for surface energy calculation; SEM and TEM images of the nanorods. See DOI: 10.1039/c4ce02431a

followed by thermal treatment. This method has been highly effective in reducing thermal conductivity compared to the bulk ingot of the same material.[18] Interestingly, the effect of grain boundary becomes more pronounced when the shape-controlled nanopowder is used instead.[19] Here, we propose an attractive method of synthesizing shape-controlled nanocrystals of PbTe and Bi_2Te_3, where the morphology was systematically determined by manipulating the shape of Te nanorods prior to the subsequent chemical transformation.

In this study, we show a series of interesting approaches to develop novel shape-and-morphology controlled nanocrystalline materials for thermoelectric application. First, we employed density-functional theory (DFT) calculations to predict how an isovalent element can modify the Gibbs surface free energy of facets in Te nanorods. Second, we synthesized shape-controlled Te nanorods, reporting other important observation in regard to the growth kinetics as well. Lastly, we successfully transformed the shape-controlled Te nanorods into PbTe and Bi_2Te_3 nanorods without losing the initial morphology. These transformed nanorods are found to have multiple nanograins inside, which clearly shows the great potential of these shape-controlled nanorods for achieving amplified multiscale phonon scattering in composite thermoelectric materials.

2. Experimental details

Materials

Te nanorods with or without Se doping were prepared by modifying the polyol process reported previously.[20,21] The chemicals used in this study were telluric acid ($Te(OH)_6$, 99%, Aldrich), selenous acid (H_2SeO_3, 99%, Aldrich), bismuth nitrate pentahydrate ($Bi(NO_3)_3{\cdot}5H_2O$, 99%, Aldrich), lead acetate trihydrate ($Pb(C_2H_3O_2)_2$, 99.99%, Aldrich), sodium hydroxide(NaOH, 93–99%, Duksan), polyvinylpyrrolidone (PVP, M_W = 55 000, 99%, Aldrich), aqueous hydroxylamine solution (50 wt% in DI water, Aldrich), acetone (≥99.8%, Aldrich), and ethylene glycol (EG ≥ 99%, J. T. Baker). DI water used in this study was obtained by using an 18 MΩ (SHRO-plus DI) system.

Monitoring the growth kinetics of Te nanorods by injecting Se during Te growth

Telluric acid (1.5 mmol), sodium hydroxide (4 mmol), and PVP (0.3 g) were dissolved in 75 ml of EG. Ethylene glycol (EG) is a polar solvent widely used in the polyol synthesis method. PVP is a widely used surfactant for nanomaterial synthesis. PVP effectively decreases the surface energy of the Te(10$\bar{1}$0) facet, enabling high aspect ratio 1-D growth of Te nanorods. Hydroxylamine aqueous solution (2.4 ml) was added to 75 ml of ethylene glycol at room temperature. The molar concentration of hydroxylamine in the reaction batch was 0.470 M. The temperature of the solution was raised to 100 °C within 3 min. The color of the solution changed to dark brown at 80 °C, indicating that nucleation of the Te nanorods began.[22] A solution of selenous acid (30 μmol) dissolved in 5 ml of EG was injected at 10, 20, and 40 min after the temperature reached 80 °C. The fraction of Se precursor *versus* Te precursor (α), ($\alpha \equiv n_{\text{Se precursor}}/(n_{\text{Se precursor}} + n_{\text{Te precursor}}) \times 100\%$), was 2.0% for this case. After 160 min from the time when the color of the solution changed to dark brown, additional telluric acid solution (1.5 mmol dissolved in 20 ml of EG) was introduced into the solution. Small amounts of samples (0.5–1 ml) were taken from the reacting solution at different reaction times (10, 20, 40, 80, 160, 170, 180, 200, 240, 280, and 320 min). The sample solutions were quenched to RT in iced water. The resulting Te nanorods in the samples were centrifuged and washed 3 times with a mixture solution of acetone and water (5 : 1, v/v). The dimensions (length and diameter) of the nanorods were obtained from SEM images by measuring more than 20 nanorods in each sample.

Verifying the unreacted precursor after 150 min of Te growth

After 150 min of Te growth with/without Se injection, the solution was centrifuged at high speed (12 000 rpm), and the supernatant solution was collected in a new flask. An excess amount of reductant (5 ml of aqueous hydroxylamine solution) was added to the supernatant solution in the new flask producing possible Te nanoparticles. The temperature was raised to 120 °C, and the reaction was maintained for 60 min to complete the reaction. The Te nanoparticles were collected by centrifugation to check the amount of unreacted Te in the first Te growth.

Synthesis of Se_xTe_y nanorods

Telluric acid (1.5 mmol), sodium hydroxide (4 mmol), and PVP (0.3 g) were dissolved in 100 mL of EG in a 250 mL three-neck round-bottom flask with a condenser. Diverse amounts of selenous acid was added to the solution. The molar fraction (α) of Se precursor *versus* Te precursor was 0, 0.3, 0.7, 1.0, and 2.0%. Nitrogen purging was applied in the solution for 30 min. Then, 2.4 ml of hydroxylamine solution (50 wt% in DI water, 0.470 M) was added to the flask. The temperature of the flask was raised to 160 °C under nitrogen purge and was held for 2 h. After reaction, the solution was cooled down to room temperature and centrifuged at 11 000 rpm for 10 min and washed three times by repeated cycles of dispersion and centrifugation in a mixture of acetone and DI water (5 : 1, v/v).

Dimension control of Te nanorods

To demonstrate the dimension control of Te nanorods, relatively thick (50 nm) and thin (20 nm) Te nanorods and also relatively short (300 nm) and long (500 nm) Te nanorods were synthesized. To obtain thin and short Te nanorods, the Se precursor (75 μmol in 5 ml of EG) was injected at 100 °C after allowing 5 min of Te growth. For thin and long Te nanorods, Te nanorods were grown without any Se injection. Thick and short nanorods were obtained by adding the Se precursor (30 μmol in 5 ml of EG) at the beginning of Te

growth. For thick and long Te nanorods, additional telluric acid (1.47 mmol) was added to the solution of thick and short nanorods after 160 min of reaction. All the reactions were maintained for 1 h to finish the reaction completely. Note that a uniform growth time of 1 hour is given for growing Te nanorods, except for the growth kinetics study as explained earlier in this section.

Chemical transformation of the Te nanorods into Bi_2Te_3 nanorods

The chemical transformation was carried out at 160 °C. A stoichiometric amount of Bi precursor (bismuth nitrate pentahydrate ($Bi(NO_3)_3{\cdot}5H_2O$)) was dissolved in 20 ml of EG. The precursor solution was injected into the reaction batch in which dimension-controlled Te nanorods were synthesized. Thin (20 nm) and short (<300 nm), thin (20 nm) and long (>500 nm), thick (50 nm) and short (<300 nm), and thick (50 nm) and long (>500 nm) Te nanorods were used for chemical transformation. The transformation reaction was quickly completed within 5 min, but the reaction was allowed for over 12 h for complete conversion. The products were centrifuged and washed three times with acetone and water.

Chemical transformation of the Te nanorods into PbTe nanorods

The experimental procedure for chemical transformation into PbTe nanorods was identical to the case of Bi_2Te_3 nanorods. A stoichiometric amount of lead acetate trihydrate ($Pb(C_2H_3O_2)_2$) was used as a metal precursor, and its solution was injected into the reaction batch in which dimension-controlled Te nanorods were synthesized. Thin and long and thick and short Te nanorods were used for chemical transformation.

Characterization

Scanning electron microscopy (SEM) was run using a JEOL JSM-7001F field-emission scanning electron microscope operated at 15 kV. Transmission electron microscopy (TEM) analysis was conducted using JEOL models (JEM-2010 and JEM-2100F) operated at 200 kV. X-ray diffraction was carried out using a RIGAKU Ultima IV.

Theoretical methodology

Theoretical calculations of the surface energy as a function of the dopant concentration were performed with first-principles density-functional theory (DFT) coupled with a thermodynamic shape model. The DFT calculations were carried out using the Vienna *ab initio* Simulations Package (VASP 5.3) code.[23,24] The ion–electron interactions were obtained *via* the projector augmented wave (PAW) method,[25,26] and the approximation to the exchange correlation was made using the Perdew, Burke, and Ernzerhof (PBE) functional.[23] The electronic wave functions were expanded in a plane-wave basis set with a kinetic energy cutoff of 500 eV. The ***k***-space integration was performed using a Monkhorst–Pack type (5 × 5 × 3) grid in the Brillouin zone for bulk Te and Se, (3 × 3 × 1) for the $p(2 \times 2)$ Te(0001) surfaces and (5 × 4 × 1) for $p(2 \times 2)$ Te($10\bar{1}0$) to ensure well-converged results within 10 meV/atom. A Methfessel–Paxton smearing of 0.1 eV was used to improve the convergence of the calculations, and the total energy was extrapolated back to zero temperature. In this work, we have also adopted the Grimme's scheme (DFT-D2)[27] to account for weak van der Waals forces in the Se/Te systems.

The most stable surface minimizes the surface Gibbs free energy as defined by $\gamma(\mu) = [G^{surf} - \sum N\mu(p,T)]/A$, where G^{surf}, μ, N, p, and T are the Gibbs surface free energy with surface area A, the atomic chemical potential, the number of atoms, the pressure, and the temperature of the system, respectively. More details of this approach can be found in ref. 28 and 29. We used the surface energies as inputs to find the equilibrium crystal shape (ECS) in the Gibbs–Wulff theorem.[23] We extended the usual ideal gas-phase relation (which links the chemical potential to gas pressures and temperatures) to that of the ideal solution. It allows us to trace the ECS of the Te nanocrystals as a function of the Se concentration (see the ESI‡ for more details).

3. Results and discussion

3.1. Surface energy modulation by Se doping

In the crystalline structure of Te, the covalently bonded intra-chains of Te are bound together *via* van der Waals attraction in a hexagonal lattice. While the extension of the axial direction of the nanorods is promoted by the formation of chemical bonds, the growth along the radial direction is promoted by the weak interaction between strands; hence, it forms 1D structures inherently by selective atomic adsorption.[30] Both Se and Te share the three-fold screw arrangement. As we consider the interaction between the injected Se precursor and the Te nanorod facets, two different adsorption modes can be considered (Fig. 1A). Adsorption of Se on Te(0001) can be viewed as an extension to the existing covalent bond, while Se on Te($10\bar{1}0$) corresponds to bond formation by van der Waals forces. As expected, the results showed relatively strong adsorption of Se on Te(0001) at low surface coverage (θ_{Se}), where θ_{Se} is the number of adsorbed Se atoms divided by the number of atomic binding sites at the outermost surface monolayer (ML) of a facet (Fig. 1B). The adsorption was found to be endothermic as it reached full surface coverage (θ_{Se} = 1.0) due to the strain sourced from the difference in the lattice parameter between Se and Te. In the prism plane modeled as Te($10\bar{1}0$) , the long-bridge site (LB) provided the preferred adsorption for Se over the short-bridge site (SB), and the adsorption energy did not vary much even though it reached full coverage.

Fig. 1C shows G^{surf} with respect to varying atomic fraction of Se (X_{Se}) at the surface *versus* the total atoms, $X_{Se} \equiv N_{Se}^{surf}/(N_{Se} + N_{Te}) \times 100\%$, where N_{Se}^{surf} is the number of Se

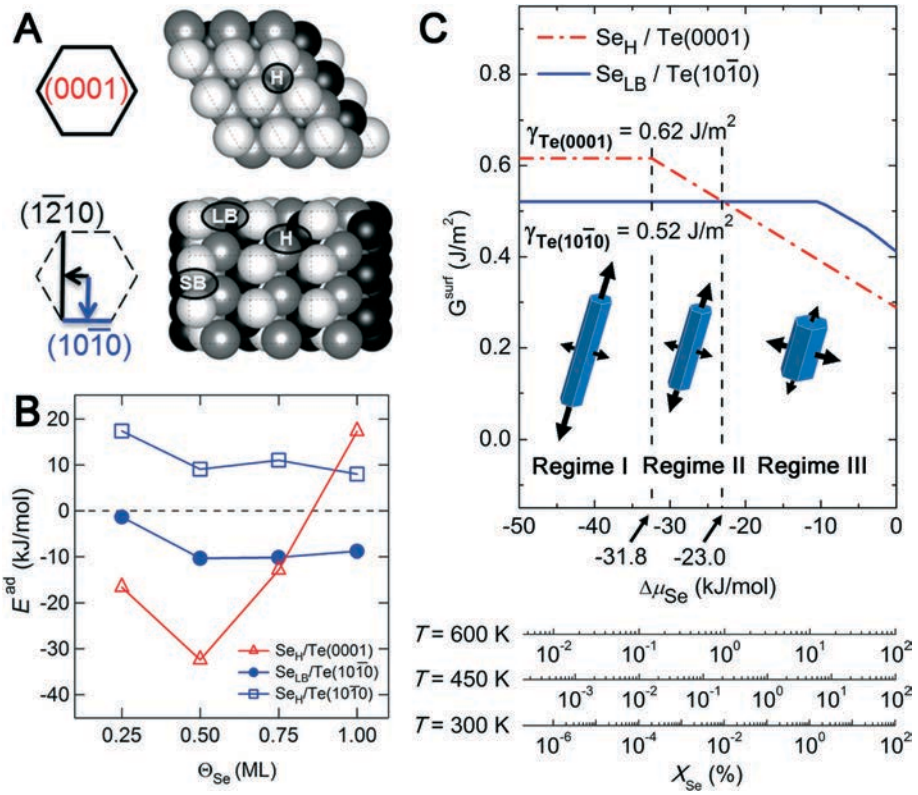

Fig. 1 (A) Atomic illustration of the Te(0001) facet and Te(10$\bar{1}$0) facet. The adsorption sites are denoted as H: hollow, LB: long bridge, and SB: short bridge sites. (B) Binding energy of Se atoms with respect to varying coverage. (C) Gibbs surface free energy of the two facets as a function of the chemical potential of Se atoms.

atoms at the surface, and N_{Se} is the total number of Se atoms in the nanorod. In this calculation, Se atoms stay only on the Te surface, hence $N_{Se} + N_{Te} \cong N_{Te}$. This assumption works well for most surface doping cases because N_{Se} is negligible compared to N_{Te}. G^{surf} of the Te(0001) facet remains the same and larger than that of the Te(10$\bar{1}$0) facet at small X_{Se} values (regime I). It starts to decrease and becomes the same or comparable with G^{surf} of the Te(10$\bar{1}$0) facet (regime II). It becomes smaller than G^{surf} of the Te(10$\bar{1}$0) facet at higher X_{Se} (regime III). The corresponding X_{Se} values depend on the reaction temperature. For example, at 450 K, the decrease in G^{surf} of the Te(0001) facet takes place at X_{Se} = 0.02%, and the crossover of G^{surf} happens at X_{Se} = 0.21%. The calculation indicates that a small amount of Se doping may lead to a significant change in the anisotropic bonding character of the Te nanorod and, by extension, to the shape of the Te product. In regime I, Te nanorods preferentially grow along the Te(0001) direction to form thin long Te nanorods. In regime II, the reduced G^{surf} slows down the axial growth rate of Te nanorods; hence, a small amount of Se doping produces shorter nanorods with a similar thickness to that of pure Te nanorods. In regime III, G^{surf} of the Te(10$\bar{1}$0) facet is lower than that of the Te(0001) facet; therefore, the elemental deposition takes place mainly on the radial direction, producing thick short nanorods. Based on the results, we predicted that a minute amount of Se dopant can manipulate the growth kinetics of Te nanorods.

While the surface and adsorption models had not included the surfactant or solvent specifically, the presence of surfactants such as PVP used in the study may play a role in shape control. To provide an estimate of this possible influence, an implicit solvation model, which simulates the dielectric interaction between the surfactant and the nanocrystal facets, has been employed. From our calculated results (see the ESI‡) within this implicit solvation approximation, we find that the solvation effects due to PVP or DI water do not change the conclusions drawn. However, it is important to mention that the effect of surfactants may be dominant over the effect of the isovalent dopant examined in this study; therefore, we stress that the interpretation of such effects should be handled with care.

3.2. Growth kinetic control of Te nanorods

In order to examine the effect of Se dopant as well as our predicted morphology change, we conducted experiments to achieve shape control of Te nanorods by pulsed supply of Se during the growth of Te nanorods. To give a realistic estimation to X_{Se}, the molar percent of the injected Se precursor ($\alpha \equiv n_{Se\ precursor}/(n_{Se\ precursor} + n_{Te\ precursor}) \times 100\%$) was used, where $n_{Se\ precursor}$ and $n_{Te\ precursor}$ are the moles of Se precursor and Te precursor added in the solution. It is notable that α is the molar ratio of the precursors, while X_{Se} is the molar fraction of reduced Se atoms *versus* reduced Te atoms. α is a

fixed value, but X_{Se} changes during the synthesis. If the reaction takes place in a batch including both precursors, X_{Se} can be similar to α during the synthesis, provided the reduction rates of the precursors are similar. We assumed that X_{Se} is the same in the mixed state of on-surface and sub-surface adsorption (which is called a "surface alloy"). At room temperature, hydroxylamine solution (2.4 ml, 0.470 M) was introduced in an EG solution (75 ml) containing telluric acid (1.5 mmol), sodium hydroxide (4 mmol), and PVP (0.3 g). The temperature of the solution was raised to 100 °C within 3 min. Nucleation of the Te nanorods apparently began at 80 °C as indicated by the change in color of the solution to deep brown, which is previously reported.[22] The temperature was considered as the starting point of the reaction in this study. The time taken to increase the solution temperature from 80 °C to 100 °C was about 60 s, so this definition does not cause a meaningful difference in analyzing the results. A solution of selenous acid (30 μmol dissolved in 5 ml of EG, α = 2.0%) was injected at 10, 20, and 40 min after the starting point of the reaction of Te. When the Se precursor is injected in a reaction batch in which Te nanorods grow, the Se precursor started to be reduced and the concentration of the reduced Se atoms increases. If the reduction of the Se precursor is not very fast, X_{Se} increases from 0 to a number larger than α because Te atoms have been consumed already for nucleation and growth. If the reduction of the Se precursor is fast, X_{Se} quickly reaches a value larger than α. Because the reduction rate of the Se precursor in this study was mild, Se precursor injection in the middle of pure Te growth started from regime II and then entered regime III as the reaction proceeded. After 160 min, a telluric acid solution (1.5 mmol dissolved in 20 ml of EG) was additionally introduced into the solution. It was aimed to investigate whether the axial growth can be activated again if the Se fraction (X_{Se}) in the solution moves from regime II to regime I again. To check the length of Te nanorods, a small amount of the sample (0.5–1 ml) was taken from the reacting solution, and the sample solutions were quenched to RT in iced water. Sampling was performed at diverse reaction times (10, 20, 40, 80, 120, 160, 170, 180, 200, 240, 280, and 320 min).

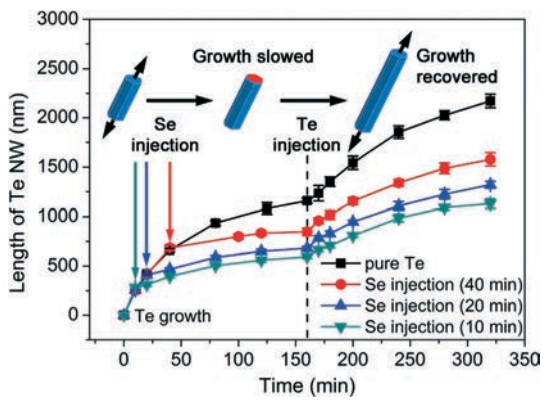

Fig. 2 Kinetic study of the length of Te nanorods affected by pulsed injection of Se precursor in the middle of Te growth. Four solution batches were prepared, and the time of Se injection was varied (indicated by arrows): no Se injection (black) and Se injection at 10 min (green), 20 min (blue), and 40 min (red). Additional Te precursor was injected in the batches after 160 min reaction time.

Fig. 2 summarizes the length change of Te nanorods during the kinetic study. Some representative SEM images of the nanorods taken after 10, 160, and 320 min are shown in the ESI‡ (Fig. S1). The growth of pure Te nanorods could be described by a first-order reaction, $dl/dt = A(C_{o,Te} - Bl)$, where l is the length of the Te nanorods (nm), A is the growth coefficient (nm L min^{-1} mol^{-1}), and B is the apparent coefficient of precursor consumption (mol nm^{-1} L^{-1}). We assumed a growth rate proportional to the precursor concentration, a constant diameter of the Te nanorods, and no additional nucleation upon injection of Se or additional Te precursors. The length (l) at a certain time and the length of the final product (l_∞) are expressed as $l = (C_o/B)[1 - e^{-ABt}]$ and $l_\infty = C_o/B$. The data in Fig. 2 were fitted with a first-order equation to obtain values of A and B that are shown in Table 1. Larger values of B indicate a larger amount of atomic consumption per unit length (Δl), that is, thicker Te nanorods or more atomic adsorption onto the radial facets. B is found to increase only after Se injection. Earlier injection (after 10 min) gave a smaller B value because X_{Se} is relatively low due to the large amount of unreacted Te atoms in the solution. The doped Se atom injection reduced the growth rate in the axial direction, which corresponds to regime II. After the second Te precursor injection, a sharp increase in Te elemental concentration (sharp decrease in X_{Se}) caused an increase in the surface energy of the growth tip again and the length grew further (regime I). The relative growth of the length can also be quantified with an increase in the A value.

We used TEM images to track the thickness change. Average thickness values were obtained from more than 10 nanorods for each thickness. The thickness changes and their normalized profiles are shown in Fig. 3. The corresponding TEM images are found in Fig. S2.‡ The normalized thickness profiles of the Te nanorods without and with Se doping did not show a meaningful difference, while the lengths of the nanorods show a large difference (Fig. 2). The results indicate that the doped Se on the growth tip (0001) of Te nanorods selectively reduces the surface energy of the growth tip but not the surface energy of the radial surfaces. Therefore, Se doping reduced the growth rate in the axial direction but did not change the growth rate in the radial direction. The reduced growth rate in the axial direction indicates that there should be a large amount of Te elements in the solution phase even after a long reaction time. Fig. S3 in the ESI‡ shows the Te nanorods that were obtained from the supernatant of a Se-doped solution. Se was doped after 10 min reaction of the Te nanorods, and the reaction was allowed to proceed for 150 min. The solution was centrifuged, and the supernatant solution was transferred into another reaction batch. An excess amount of reductant (5 ml of hydroxylamine solution, 50 v/v%) was added to the new reaction batch. The temperature was raised to 120 °C, and the reaction was maintained for 60 min. It is notable that the reaction batch without Se doping

Table 1 Growth coefficient (A) and the coefficient of precursor consumption (B) of Te nanorods

	Pure Te		Se injection (10 min)		Se injection (20 min)		Se injection (40 min)	
	A	B ($\times 10^{-6}$)	A	B ($\times 10^{-6}$)	A	B ($\times 10^{-6}$)	A	B ($\times 10^{-6}$)
Before Se injection	14 000	1.2	—	—	—	—	—	—
After Se injection	—	—	3000	4	3000	5	2000	7
After Te injection	7000	1.1	4500	2.3	4700	1.7	6000	1.6

contained a negligible amount of unreacted Te (<1% of injected precursor) after 150 min, so the supernatant solution produced a negligible amount of Te under the same reduction conditions (Fig. S8‡).

More dramatic control of dimensions could be obtained by adjusting the value of α; Fig. 4 shows the results. In order to remove the kinetic effect on the dimensions of the product, the Se precursor was mixed with the Te precursor from the beginning of Te growth. Because the Se precursor is reduced faster than the Te precursor, X_{Se} at the early stage is higher than the relative precursor concentration (α). The value of α was varied in the range of less than 2.0% (α = 0, 0.3, 0.7, 1.0, 2.0%). For the experiments, telluric acid (1.5 mmol), sodium hydroxide (4 mmol), and PVP (0.3 g) were dissolved in 100 mL of EG. Selenous acid with diverse α (α = 0, 0.3, 0.7, 1.0, 2.0%) was added to the solution. Then, the precursors were reduced by 2.4 ml of hydroxylamine solution. The color of the solution did not change at room temperature, which indicates that nucleation of the nanorods did not take place. The temperature of the flask was raised to 160 °C under nitrogen purging and was held for 2 h.

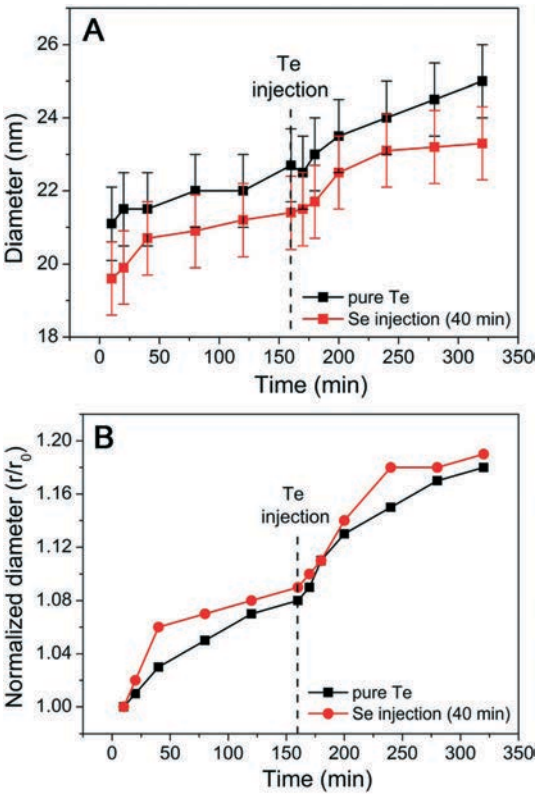

Fig. 3 Kinetic study of the diameter of Te nanorods affected by pulsed injection of Se precursor in the middle of Te growth. (A) Diameter profile and (B) normalized diameter profile. Two solution batches were prepared, and the time of Se injection was varied: no Se injection (black) and Se injection at 40 min (red). Additional Te precursor was injected in the batches after 160 min reaction time.

The shape and microstructural details of the resulting Te nanorods were characterized by transmission electron microscopy (TEM) (Fig. 4). Fig. 3A–C show the Te nanorods at α = 0, 0.3, and 2.0%, respectively. Te nanorods showed the typical trigonal structure based on high-resolution TEM (HRTEM). Fig. 4D was taken from a sample with α = 2.0%. The lattice indices and structure were identical to that of the HRTEM images and XRD (ESI,‡ Fig. S4) at any α value (α < 2.0%). Fig. 4E summarizes the dimensions of the resulting Te nanorods. The thickness of Te nanorods sharply increased from 26 nm to 71 nm, while the length drops from 800 nm to 337 nm. The changes in nanorod dimensions were not significant when α was larger than 0.3%. Based on these dimensions of the nanorods, the volume was then calculated; hence, the number of nuclei was deduced and obtained as a function of α (Fig. 4F). At α = 0.3%, the number of nuclei was found to be reduced to half that of pure Te. The small number of nuclei resulting in thicker nanorods indicates that a higher concentration of Se precursor might suppress the formation of nuclei of Te nanorods, while the effect of shape control is strongly amplified. The observed dimensional changes imply that the reaction mechanism corresponds to regime III at $\alpha > 0.3\%$.

3.3. Chemical transformation into M_xTe_y 1D nanomaterials

Dimension control is critical in defining the properties of nanostructured materials. The results in Fig. 4 indicate that the dimensions of the Te 1D nanostructured materials may be precisely controlled. As an example of producing functional nanorods and nanorods with controlled dimensions, we chemically transformed the dimension-controlled Te nanorods into thermoelectric materials such as Bi_2Te_3, PbTe nanorods and nanorods. Chemical transformation of Te template nanowires into Pt nanotubes and Pd nanowires was reported.[31] Bi_2Te_3 has a relatively high electrical conductivity and low thermal conductivity; therefore, it has been widely used for small-scale cooling components and low-temperature power generators.[32,33] PbTe also presents a possibility for competitive thermoelectric devices in the high temperature region.[34] To increase the thermoelectric figure

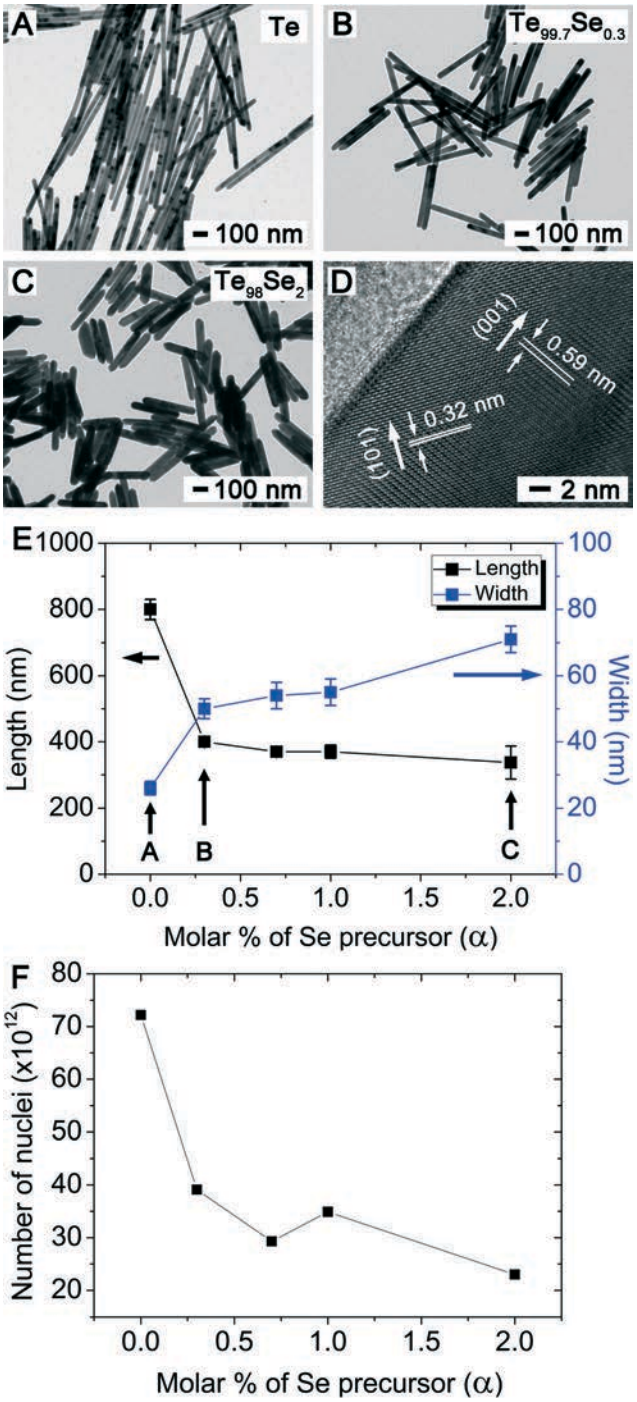

Fig. 4 TEM image of Se-doped Te nanorods with respect to molar percent of Se precursor (α) ($\alpha \equiv$ ([Se precursor]/([Se precursor] + [Te precursor]) × 100%): (A) 0%, (B) 0.3%, and (C) 2.0%. (D) High-resolution transmission microscopy (HRTEM) image of a Te nanorod with α = 2.0%. (E) Change in the length and diameter of the Te nanorods with respect to α. (F) Number of nuclei of Te nanorods with respect to α.

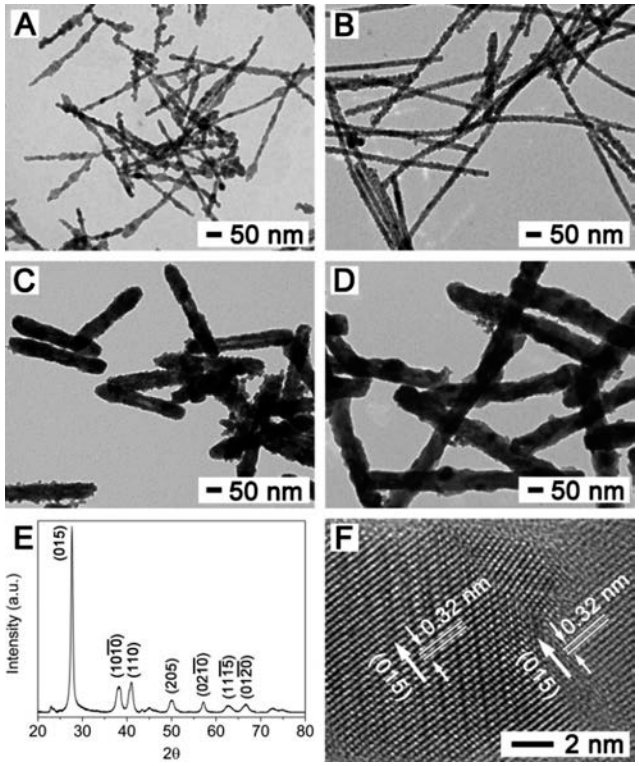

Fig. 5 (A–D) TEM images of Bi_2Te_3 nanorods chemically transformed from the dimension-controlled Te nanorods as follows: (A) Se precursor injection after 5 min of Te growth, (B) without Se injection, (C) Se precursor mixed at the beginning, and (D) additional Te injection into the solution (C). (E, F) X-ray diffraction and HRTEM of the Bi_2Te_3 nanorods in (A).

of merit, structures designed to have as many nanograins as possible have been intensively investigated.[35] Recently, it has been attracting interest as topological insulators whose unusual conductive metallic surfaces are expected to afford new spintronic devices at room temperature.[36]

Fig. 5 demonstrates different dimensions of Bi_2Te_3 nanorods transformed from the Te nanorods produced by the approach introduced in this study. To obtain thin and short Te nanorods (Fig. 5A), pulsed Se inoculation was applied in the growing Te nanorods at 100 °C by injecting selenous acid (75 μmol) dissolved in 5 ml of EG after allowing 5 min of Te growth. For thin and long Te nanorods (Fig. 5B), Te nanorods were grown without any Se injection. The thick and short nanorods (Fig. 5C) were obtained by adding the Se precursor (30 μmol) at the beginning of Te growth. Thick and long Te nanorods (Fig. 5D) were obtained by adding additional telluric acid (1.47 mmol) after 160 min of reaction. All the reactions were maintained for 4 h to finish the reaction completely. The chemical transformation was carried out at 160 °C. A stoichiometric amount of Bi precursor dissolved in 20 ml of EG was injected into the reaction batch after the synthesis of the Te nanorods was finished. The chemical transformation reaction was allowed for 1 h, although the transformation was quickly completed within 5 min. With chemical transformation temperature of 160 °C, Bi_2Te_3 reorganized into its stable trigonal structure, making its surface rough. The products were centrifuged and washed three times with acetone and water. The XRD and HRTEM images in Fig. 5E and F were obtained from the Bi_2Te_3 shown in Fig. 5B. The XRD corresponds to the rhombohedral crystal

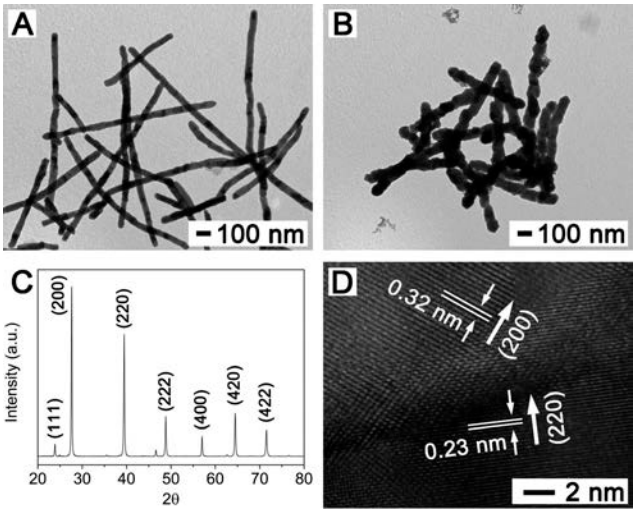

Fig. 6 (A, B) TEM images of PbTe nanorods chemically transformed from the dimension-controlled Te nanorods as follows: (A) without Se injection and (B) Se precursor mixed at the beginning, (C, D) X-ray diffraction and HRTEM of the PbTe nanorods in (A).

structure with a typical layered structure. The same XRD results were routinely obtained regardless of the dimensions of the Te nanorods, indicating the chemical transformation proceeded to completion (ESI,‡ Fig. S5). The HRTEM image exhibits the microstructure with nanosized polycrystal grains, which were seen under other conditions. Such nanograins are expected to reduce the thermal conductivity by phonon scattering.[13]

Fig. 6 also demonstrates different dimension-controlled PbTe nanorods. Synthesis of PbTe nanowires chemically transformed from Te nanowires has been reported.[37] Thin and long PbTe nanorods (Fig. 6A) and thick and short PbTe nanorods (Fig. 6B) can be prepared by the approach introduced in this study. To achieve complete conversion into PbTe, Fig. 6A was transformed at 100 °C, and Fig. 6B was transformed at 160 °C. At higher transformation temperature, PbTe nanorods reorganize into its stable rock-salt structure, making its surface rough. Reorganization of the PbTe nanorods at high temperature was observed (ESI,‡ Fig. S6). The XRD and HRTEM images in Fig. 6C and D were obtained from the PbTe shown in Fig. 6B. The same XRD results were routinely obtained regardless of the dimensions of the Te nanorods, indicating the chemical transformation proceeded to completion (ESI,‡ Fig. S7).

4. Conclusions

In this study, we have successfully demonstrated a systematic approach to synthesize chemically transformed, shape-controlled thermoelectric nanomaterials. We find that a small fraction of dopants may affect the surface energies of the crystal surfaces; hence, the growth rate of the fast growing crystal facet can be controlled. As a proof of concept, we investigated the effect of Se doping on growing Te nanorods. From our DFT calculations, the surface energy of the Te(0001) facet was lowered at a small atomic fraction (X_{Se}) of Se doping. According to the calculated surface energy change of the Te(0001) facet, three regimes were classified: fast growth in the axial direction ($X_{Se} < 0.02\%$ at 450 K, regime I) slow growth in the axial direction and no change in thickness ($0.02\% < X_{Se} < 0.21\%$ at 450 K, regime II), and preferential growth in the radial direction ($X_{Se} > 0.21\%$ at 450 K, regime III). This prediction was in excellent agreement with our experimental results. Pulsed injection of Se precursor in the middle of Te growth slowed down the axial growth of the Te nanorods but without a significant change in the thickness (regime II). Additional supply of Te precursor was found to re-initiate length-wise growth (regime I). Meanwhile, addition of a small fraction of Se precursor from the beginning of the reaction inhibited the length-wise growth, while promoting an increase in nanorod thickness (regime III). This capability for fine dimensional control was utilized to produce Bi_2Te_3 nanorods and nanorods with a polycrystal structure constructed of nanosized grains. This synthetic approach for controlling the dimensions of nanomaterials can be extended to other nanomaterial systems.

Acknowledgements

This work was supported by a National Research Foundation (NRF) grant funded by the Korean Government (MEST) through the Pioneer Research Program of KOSEF (008-05103) and the Basic Science Research Program by the NRF, (Grant No. 2014R1A1A1003415). Computational resources have been provided by the KISTI Supercomputing Center (KSC-2014-C3-062).

References

1 Y. Xia, P. Yang, Y. Sun, Y. Wu, B. Mayers, B. Gates, Y. Yin, F. Kim and H. Yan, One-Dimensional Nanostructures: Synthesis, Characterization, and Applications, *Adv. Mater.*, 2003, **15**(5), 353–389.

2 A. I. Hochbaum and P. Yang, Semiconductor Nanowires for Energy Conversion, *Chem. Rev.*, 2010, **110**, 527–546.

3 H.-S. Qian, S.-H. Yu, J.-Y. Gong, L.-B. Luo and L.-F. Fei, High-Quality Luminescent Tellurium Nanowires of Several Nanometers in Diameter and High Aspect Ratio Synthesized by a Poly(Vinyl Pyrrolidone)-Assisted Hydrothermal Process, *Langmuir*, 2006, **22**, 3830–3835.

4 R. Malakooti, L. Cademartiri, Y. Akçakir, S. Petrov, A. Migliori and G. A. Ozin, Shape-Controlled Bi_2S_3 Nanocrystals and Their Plasma Polymerization into Flexible Films, *Adv. Mater.*, 2006, **18**(16), 2189–2194.

5 Z. Liu, D. Xu, J. Liang, J. Shen, S. Zhang and Y. Qian, Growth of Cu_2S Ultrathin Nanowires in a Binary Surfactant Solvent, *J. Phys. Chem. B*, 2005, **109**, 10699–10704.

6 Q. Zhang, S.-J. Liu and S.-H. Yu, Recent advances in oriented attachment growth and synthesis of functional materials: concept, evidence, mechanism, and future, *J. Mater. Chem.*, 2009, **19**(2), 191.
7 Q. Yan, H. Chen, W. Zhou, H. H. Hng, F. Y. C. Boey and J. Ma, A Simple Chemical Approach for PbTe Nanowires with Enhanced Thermoelectric properties, *Chem. Mater.*, 2008, **20**, 6298–6300.
8 G. D. Moon, S. Ko, Y. Xia and U. Jeong, Chemical transformations in Ultrathin Chalcogenide Nanowires, *ACS Nano*, 2010, **4**(4), 2307–2319.
9 X. Peng, Mechanisms for the Shape-Control and Shape-Evolution of Colloidal Semiconductor Nanocrystals, *Adv. Mater.*, 2003, **15**(5), 459–463.
10 J. B. In, H. J. Kwon, D. Lee, S. H. Ko and C. P. Grigoropoulos, *In situ* monitoring of laser-assisted hydrothermal growth of ZnO nanowires: thermally deactivating growth kinetics, *Small*, 2014, **10**(4), 741–749.
11 Y. Min, G. D. Moon, C.-E. Kim, J.-H. Lee, H. Yang, A. Soon and U. Jeong, Solution-based synthesis of anisotropic metal chalcogenide nanocrystals and their applications, *J. Mater. Chem. C*, 2014, **2**(31), 6222.
12 M. R. Gao, Y. F. Xu, J. Jiang and S. H. Yu, Nanostructured metal chalcogenides: synthesis, modification, and applications in energy conversion and storage devices, *Chem. Soc. Rev.*, 2013, **42**(7), 2986–3017.
13 B. Poudel, Q. Hao, Y. Ma, Y. Lan, A. Minnich, B. Yu, X. Yan, D. Wang, A. Muto, D. Vashaee, X. Chen, J. Liu, M. S. Dresselhaus, G. Chen and Z. Ren, High-thermoelectric performance of nanostructured bismuth antimony telluride bulk alloys, *Science*, 2008, **320**(5876), 634–638.
14 H. J. Wu, L. D. Zhao, F. S. Zheng, D. Wu, Y. L. Pei, X. Tong, M. G. Kanatzidis and J. Q. He, Broad temperature plateau for thermsoelectric figure of merit ZT>2 in phase-separated $PbTe_{0.7}S_{0.3}$, *Nat. Commun.*, 2014, **5**, 4515.
15 L. Hicks and M. Dresselhaus, Effect of quantum-well structures on the thermoelectric figure of merit, *Phys. Rev. B: Condens. Matter Mater. Phys.*, 1993, **47**(19), 12727–12731.
16 A. I. Hochbaum, R. Chen, R. D. Delgado, W. Liang, E. C. Garnett, M. Najarian, A. Majumdar and P. Yang, Enhanced thermoelectric performance of rough silicon nanowires, *Nature*, 2008, **451**(7175), 163–167.
17 L. Hicks and M. Dresselhaus, Thermoelectric figure of merit of a one-dimensional conductor, *Phys. Rev. B: Condens. Matter Mater. Phys.*, 1993, **47**(24), 16631–16634.
18 Y. Ma, Q. Hao, B. Poudel, Y. Lan, B. Yu, D. Wang, G. Chen and Z. Ren, Enhanced Thermoelectric Figure-of-Merit in p-Type Nanostructured Bismuth Antimony Tellurium alloys Made from Elemental Chunks, *Nano Lett.*, 2008, **8**(8), 2580–2584.
19 M. R. Buck and R. E. Schaak, Emerging strategies for the total synthesis of inorganic nanostructures, *Angew. Chem., Int. Ed.*, 2013, **52**(24), 6154–6178.
20 B. Mayers and Y. Xia, Formation of Tellurium Nanotubes Through Concentration Depletion at the Surfaces of Seeds, *Adv. Mater.*, 2002, **14**(4), 279–282.
21 B. Mayers and Y. Xia, One-dimensional nanostructures of trigonal tellurium with various morphologies can be synthesized using a solution-phase approach, *J. Mater. Chem.*, 2002, **12**(6), 1875–1881.
22 B. Gates, B. Mayers, B. Cattle and Y. Xia, Synthesis and Characterization of Uniform Nanowires of Trigonal Selenium, *Adv. Funct. Mater.*, 2002, **12**(3), 219–227.
23 J. P. Perdew, K. Burke and M. Ernzerhof, Generalized Gradient Approximation Made Simple, *Phys. Rev. Lett.*, 1996, **77**(18), 3865–3868.
24 G. Kresse and J. Furthmuller, Efficient Iterative Schemes for *ab-initio* Total-Energy Calculations Using a Plane-Wave Basis Set, *Phys. Rev. B: Condens. Matter Mater. Phys.*, 1996, **54**(16), 11169–11186.
25 P. E. Blöchl, Projector augmented-wave method, *Phys. Rev. B: Condens. Matter Mater. Phys.*, 1994, **50**(24), 17953–17979.
26 G. Kresse and D. Joubert, From Ultrasoft Pseudopotentials to the Projector Augmented-Wave Method, *Phys. Rev. B: Condens. Matter Mater. Phys.*, 1999, **59**(3), 1758–1775.
27 S. Grimme, Semiempirical GGA-type density functional constructed with a long-range dispersion correction, *J. Comput. Chem.*, 2006, **27**(15), 1787–1799.
28 X. Duan, O. Warschkow, A. Soon, B. Delley and C. Stampfl, Density functional study of oxygen on Cu(100) and Cu(110) surfaces, *Phys. Rev. B: Condens. Matter Mater. Phys.*, 2010, **81**(7), 075430.
29 T. Lee, B. Delley, C. Stampfl and A. Soon, Environment-dependent nanomorphology of TiN: the influence of surface vacancies, *Nanoscale*, 2012, **4**(16), 5183–5188.
30 G. D. Moon, Y. Min, S. Ko, S.-W. Kim, D.-H. Ko and U. Jeong, Understanding the Epitaxial Growth of SexTey@Te Core–Shell Nanorods and the Generation of Periodic Defects, *ACS Nano*, 2010, **4**(12), 7283–7292.
31 H.-W. Liang, S. Liu, J.-Y. Gong, S.-B. Wang, L. Wang and S.-H. Yu, Ultrathin Te Nanowires: An Excellent Platform for Controlled Synthesis of Ultrathin Platinum and Palladium Nanowires/Nanotubes with Very High Aspect Ratio, *Adv. Mater.*, 2009, **21**(18), 1850–1854.
32 Y. Min, J. W. Roh, H. Yang, M. Park, S. I. Kim, S. Hwang, S. M. Lee, K. H. Lee and U. Jeong, Surfactant-free scalable synthesis of Bi_2Te_3 and Bi_2Se_3 nanoflakes and enhanced thermoelectric properties of their nanocomposites, *Adv. Mater.*, 2013, **25**(10), 1425–1429.
33 W. Shi, L. Zhou, S. Song, J. Yang and H. Zhang, Hydrothermal Synthesis and Thermoelectric Transport Properties of Impurity-Free Antimony Telluride Hexagonal Nanoplates, *Adv. Mater.*, 2008, **20**(10), 1892–1897.
34 J. P. Heremans, V. Jovovic, E. S. Toberer, A. Saramat, K. Kurosaki, A. Charoenphakdee, S. Yamanaka and G. J. Snyder, Enhancement of thermoelectric efficiency in PbTe by distortion of the electronic density of states, *Science*, 2008, **321**(5888), 554–557.
35 M. Scheele, N. Oeschler, I. Veremchuk, K.-G. Reinsberg, A.-M. Kreuziger, A. Kornowski, J. Broekaert, C. Klinke and H. Weller, ZT Enhancement in Solution-Grown $Sb_{(2-x)}Bi_xTe_3$ Nanoplatelets, *ACS Nano*, 2010, **4**(7), 4283–4291.

36 H. Peng, K. Lai, D. Kong, S. Meister, Y. Chen, X. L. Qi, S. C. Zhang, Z. X. Shen and Y. Cui, Aharonov–Bohm interference in topological insulator nanoribbons, *Nat. Mater.*, 2010, **9**(3), 225–229.

37 H. W. Liang, S. Liu, Q. S. Wu and S. H. Yu, An efficient templating approach for synthesis of highly uniform CdTe and PbTe nanowires, *Inorg. Chem.*, 2009, **48**(11), 4927–4933.

Electronic Supplementary Material (ESI) for CrystEngComm.

Supporting Information

A. Modelling the basal plane and the prism planes of the Te nanorod

To model the prism and basal planes of the Te nanorods, we used symmetric periodic supercell slab models consisting of 3,6,9 and 12 atomic layers to find a representative model for the clean surface without Se adsorption. Finally we chose 9 atomic layers model with its five inner layers fixed. We calculated the optimized total energies of the Se/Te surface systems for various surface coverage of Se, using p(2 × 2) surface supercells, where the coverage of Se ranges from 0.25 to 1.00 monolayers (ML). In particular, the basal plane is represented by the (0001) surface of Te, while the prism plane is modeled using the $(10\bar{1}0)$ surface. These simplification is based on the crystal symmetry of Te nanorod, which has P 31 2 1 trigonal symmetry with hexagonal lattice. Covalently bonded tellurium atoms comprise a strand, and each strand forms van der Waals bonding with other strands. Its prism planes can be divided into two degenerate configurations due to its trigonal symmetry, and the two group share the same relative configuration due to the two fold symmetry. Therefore $(10\bar{1}0)$ facet alone can represent other five prism planes altogether. We also tested surface energy of $(\bar{1}2\bar{1}0)$ plane groups as well, and found that $(10\bar{1}0)$ gives lower surface free energy which means the better stability. This can be explained by the fact that the number of cut-off covalent bond is minimized for the planes belong to $\{10\bar{1}0\}$ family.

In order to estimate the effect of the surfactant and solvent environment, we used an *implicit* solvation model to calculate the solvation free energy due to the dielectric interaction between the surface and the surfactant, as implemented in VASPsol program.[S01] We approximated the relative dielectric constant of 4.0 to represent PVP, and 80.0 to represent deionized water in direct contact with the different facets. From the calculations, it is found that the solvation effect due to dielectric interaction is nominal in the Gibbs surface free energy results used in the main text. (see Figure S0 below) Still, it should be noted that the *explicit* role of PVP upon modifying the morphology of nanocrystal is not fully addressed in this *implicit* solvent model, such as selective binding effect.[S02]

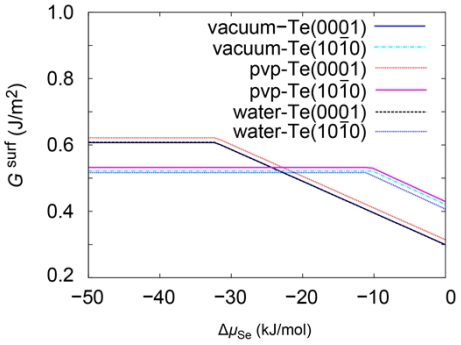

Figure S0. Solvation effect-induced Gibbs surface free energy diagram, due to chemical species in the reaction environment (PVP and DI-water), as described by the implicit solvation model. The relative dielectric constant of 4.0 is used for PVP, and 80.0 for DI-water.

B. Derivation to the calculation of the Gibbs surface free energy, Wulff shape, and the corresponding mole fraction of Selenium.

Adsorption energy per selenium atom:

$$E^{ad}(hktl,\theta,n^{Se}) = \frac{1}{n^{Se}}\left(E^{Se|Te}(hktl,\theta) - E^{Te}(hktl) - n^{Se}E^{Se}_{bulk} \right)$$

Where *hktl* denotes the Miller-Bravais 4-axis notation, and $t = -(h+k)$.

The surface of a tellurium facet can be calculated from the slab model as,

$$\sigma(hktl,\theta,s,n^{Se}) = \frac{1}{2A}\left(E^{Se|Te}(hktl,\theta,s) - E^{Te}(hktl) - n^{Se}E^{Se}_{bulk} \right)$$

where $\sigma(hktl)$ is the surface energy, $E^{Se|Te}(hktl,\theta)$ is the calculated total energy from DFT calculation for the Te(hktl) slab models with selenium atoms on the adsorption sites, θ is coverage in a unit of monolayer(ML), *s* is the variable for the adsorption site, $E^{Te}(hktl)$ is the total energy of the clean Te(hktl) slab, n^{Se} is the number of selenium atoms, E^{Se}_{bulk} is the reference energy for the adsorped selenium atom, which is taken to be the bulk phase of Se in this study.

Change in the Gibbs surface free energy with respect to varying chemical potential of the components can be expressed as following,

$$\Delta G^{surf}(hktl,\theta,s,n^{Se},\Delta\mu^{Se}) = \frac{1}{2A}\left(E^{Se|Te}(hktl,\theta,s) - E^{Te}(hktl) - n^{Se}\Delta\mu^{Se} - n^{Te}\Delta\mu^{Te} \right)$$

Note that "Change" refers to the change in Gibbs surface free energy due to adsorption of Selenium on the clean surface.

Therefore the full expression for the total Gibbs surface free is,

$$G^{surf} = \sigma + \Delta G^{surf}$$

Here we consider the change of chemical potential only for the adsorbate. Thus we approximated $\Delta\mu^{Te} \approx 0$.

Define the change in chemical potential of the Selenium with respect to its reference, (in this case, bulk Selenium) then it can be expressed as:

$$\Delta\mu^{Se} = \mu^{Se} - E^{Se}_{ref} = \mu^{Se} - E^{Se}_{bulk}$$

Reference values can be varied depending on the chemical conditions, and therefore one should not misinterpret the meaning of the zero value in the axis of chemical potential (*x*-axis). Since we set an approximation of invariable chemical potential of Te, therefore extremely high level of chemical potential of selenium will not represent the pure selenium state.

Now the change in Gibbs surface free energy can be expressed as:

$$\Delta G^{surf}\left(hktl, \theta, s, n^{Se}, \Delta\mu^{Se}\right) = \frac{1}{2A}\left(E^{Se|Te}(hktl, \theta, s) - E^{Te}(hktl) - n^{Se}(\Delta\mu^{Se} + E^{Se}_{bulk}) \right)$$

Mind that,

$$E^{ad}(hktl, \theta, s, n^{Se}) = \frac{1}{n^{Se}}\left(E^{Se|Te}(hktl, \theta, s) - E^{Te}(hktl) - n^{Se}E^{Se}_{bulk} \right)$$

We take the same reference of Selenium chemical potential reservoir in this study (i.e. bulk Selenium), Therefore,

$$\Delta G^{surf}\left(hktl, \theta, s, n^{Se}, \Delta\mu^{Se}\right) = \frac{n^{Se}}{2A}\left(E^{ad}(hktl, \theta, s, n^{Se}) - \Delta\mu^{Se} \right)$$

and,

$$G^{surf}\left(hktl, \theta, s, n^{Se}, \Delta\mu^{Se}\right) = \sigma(hktl) + \Delta G^{surf}\left(hktl, \theta, s, n^{Se}, \Delta\mu^{Se}\right)$$

$$= \sigma(hktl) + \frac{n^{Se}}{2A}\left(E^{ad}(hktl, \theta, s, n^{Se}) - \Delta\mu^{Se} \right)$$

By this, the Gibbs surface free energy has been derived as a linear function with respect to change in the chemical potential of selenium, $\Delta\mu^{Se}$.

From the equation, we can define multiple number of linearly decreasing G^{surf} functions, but we are only interested in the one with the lowest possible energy values. Therefore the observed Gibbs surface free energy can be derived as,

$$\bar{G}^{surf}\left(hktl, \theta, s, n^{Se}, \Delta\mu^{Se}\right) = \sigma(hktl) + M(\Delta\mu^{Se})$$

where,

$$M(\Delta\mu^{Se}) = min\left\{\frac{n^{Se}}{2A}\left(E^{ad}(hktl, \theta, s, n^{Se}) - \Delta\mu^{Se} \right)\right\}_{\Delta\mu^{Se} < 0}$$

From these results, we can define the relationship between the thermodynamic descriptions of the surface energy of individual tellurium facet with respect to varying chemical potential of selenium in the chemical environment.

From the former discussion, we discuss two important calculation results, which correspond well with our experimental observations.

Firstly, the equilibrium crystalline shape (ECS) can be estimated by the Wulff construction. [S03]

$$\Delta G_i = \sum_j \sigma_j A_j$$

Where σ_j is the surface energy of j^{th} facet, and A_j is the area of the facet. From this definition, one can define a hypothetical construction in which exterior facets having normal vectors pointing to an origin, with the length of the j^{th} normal vector h_j as,

$$h_j = \lambda \sigma_j$$

And then the shape represents an equilibrium crystalline shape to which thermodynamic driving force exist.

Secondly, we provide a useful interpretation of the chemical potential change in terms of the mole fraction of the selenium used in the experiment.

We describe the chemical potential of i^{th} element in terms of chemical activity,

$$\mu^i = \mu_o^i + RTlna^i$$

where we used the ideal gas constant $R = 8.3144621\, J \cdot K^{-1} \cdot mol^{-1}$, T is the temperature, and the a^i is the chemical activity. The change in the chemical potential of selenium is,

$$\Delta\mu^{Se} = \mu^{Se} - \mu_{ref}^{Se}$$

Here, $\Delta\mu^{Se}$ is zero when the chemical potential of selenium reaches that of its reference state, which is, bulk state in this result. Then that can be expressed as,

$$\Delta\mu^{Se} = RTlnX^{Se}$$

where it reaches zero when X^{Se} reaches one. Here we used the ideal gas constant for simplicity.

Finally, the mole fraction of X^{Se} can be calculated by,

$$X^{Se} = exp(\frac{\Delta\mu^{Se}}{RT})$$

[S01] K. Mathew, R. Sundararaman, K. Letchworth-Weaver, T. A. Arias, and R. G. Hennig, J. Chem. Phys. **140**, 084106 (2014).

[S02] P. S. Mdluli, N. M. Sosibo, P. N. Mashazi, T. Nyokong, R. T. Tshikhudo, A. Skepu, and E. Van Der Lingen, J. Mol. Struct. **1004**, 131 (2011).

[S03] G. Wulff, Zeitschrift für Kristallographie-Crystalline Materials **34**, 449 (1901).

C. Experimental Section

Materials. The chemicals used in this study were telluric acid ($Te(OH)_6$, 99 %, Aldrich), selenous acid (H_2SeO_3, 99 %, Aldrich), bismuth nitrate pentahydrate ($Bi(NO_3)_3{\cdot}5H_2O$, Aldrich), sodium hydroxide(NaOH, 93~99 %, Duksan), polyvinylpyrollidone (PVP, $M_W \fallingdotseq$ 55,000, 99 %, Aldrich), hydroxylamine solution(w.t. 50 % in D. I. water, Aldrich), acetone (≥99.8 %, Aldrich), ethylene glycol (EG ≥99 %, J. T. Baker). D. I. water was obtained by an 18-MΩ (SHRO-plus DI) system.

Synthesis of Se_xTe_y alloys. To synthesize Se_xTe_y alloys, solvothermal method was used. Telluric acid and selenous acid (1.5 mmol in total with molar ratio $Te(OH)_6/H_2SeO_3$ = 100: 0, 99.7: 0.3, 99.3: 0.7, 99: 1 and 98: 2) were used as metal precursors. Sodium hydroxide (0.2 g (4 mmol)) and PVP (0.3 g (2.7 mmol)) were used. Above reagents were dissolved into 100ml of EG and poured into 250 ml round-bottom flask and stirred for 5 min for perfect mixture formation. Then 2.4 ml of hydroxyl amine solution were added at room temperature and flask was sealed with septa. Temperature was raised to 160 ^oC under nitrogen purging atmosphere and kept for 2 hours. After reaction, the solution was cooled down to room temperature and centrifuged (11,000 rpm, 10 min) 3 times using acetone (500 ml) and D. I. water (100 ml).

Kinetic observations. For observe kinetics of tellurium nanowire growth, telluric acid (0.345 g (1.5 mmol)), sodium hydroxide (0.2 g (4 mmol)) and PVP (0.3 g (2.7 mmol)) in 75 ml of EG were used for initial stage reaction. Hydroxylamine solution (2.4 ml) was mixed at room temperature and temperature was raised to 100 ^oC under nitrogen environment. Starting point of the reaction was set as the point of the solution temperature of 80 ^oC. Additional selenous acid (3.87 mg (30 μmol) in 5 ml of EG) was injected at 10/20/40 min after reaction starting point. Then, telluric acid (0.345 g (1.5 mmol) in 20 ml of EG) was injected into reaction mixture 160 min after reaction starting point. 0.5~1 ml of solution was taken out from reacting flask at 10/20/40/80/120/160/170/180/200/240/280/320 min and quenched down to R.T. and centrifuged 3 times for obtaining length profile through SEM observation. After reaction, the solution was cooled down to room temperature and centrifuged 3 times.

Formation of $Bi_2Se_xTe_y$ structures. For chemically transformed bismuth telluride structures, two-step procedure was used. First, Se_xTe_y alloys with various lengths and thicknesses were synthesized using morphology-controlling method introduced through this paper. After then bismuth precursor with stoichiometric ratio was injected for chemical transformation. In every case in **Figure 4**, basic experiment condition was identical to the kinetic observations part except reaction temperature of

100°C. To obtain thin and short case, selenous acid (9.675 mg (75 μmol) in 5 ml of EG) was injected at 5 min after reaction starting point. For thin and long case, tellurium nanorods are grown without any selenium injection. Thick and short case was obtained by using selenous acid (3.87 mg (30 μmol) and telluric acid (0.338 g (1.47 mmol)). Thick and long case was obtained by doing same procedure as thick and short case and after 120 min of reaction, telluric acid (0.345 g (1.5 mmol) in 20 ml of EG) was injected. All of the reactions were kept for 4 hours after final precursor injection of selenous acid or telluric acid. After then, bismuth nitrate pentahydrate (0.485 g (1 mmol) in 20 ml of EG, 0.970 g (2 mmol) for thick and long case) was injected into reacting flask and temperature was raised to 160 °C for perfect chemical transformation and kept for over 12 hours. After reaction, the solution was cooled down to room temperature and centrifuged 3 times.

Formation of $PbSe_xTe_y$ structures. For chemically transformed lead telluride structures, two-step procedure was used. First, Se_xTe_y alloys with various lengths and thicknesses were synthesized using morphology-controlling method introduced through this paper. After then lead precursor with stoichiometric ratio was injected for chemical transformation. In every case in **Figure 5**, basic experiment condition was identical to the kinetic observations part except reaction temperature of 100°C. For thin and long case, tellurium nanorods are grown without any selenium injection. Thick and short case was obtained by using selenous acid (3.87 mg (30 μmol) and telluric acid (0.338 g (1.47 mmol)). After then, lead acetate trihydrate (0.569 g (1.5 mmol) in 20 ml of EG) was injected into reacting flask and temperature was set to 100 °C (160 °C for thick and short case) for perfect chemical transformation and kept for over 12 hours. After reaction, the solution was cooled down to room temperature and centrifuged 3 times.

D. Characterizations

Scanning electron microscopy (SEM) was run on a JEOL JSM-7001F field-emission scanning electron microscope operated at 15 kV. Transmission electron microscope (TEM) analysis was conducted with JEOL models (JEM-2010 and JEM-2100F) that were operated at 200 kV. X-ray diffraction was run on a RIGAKU Ultima IV.

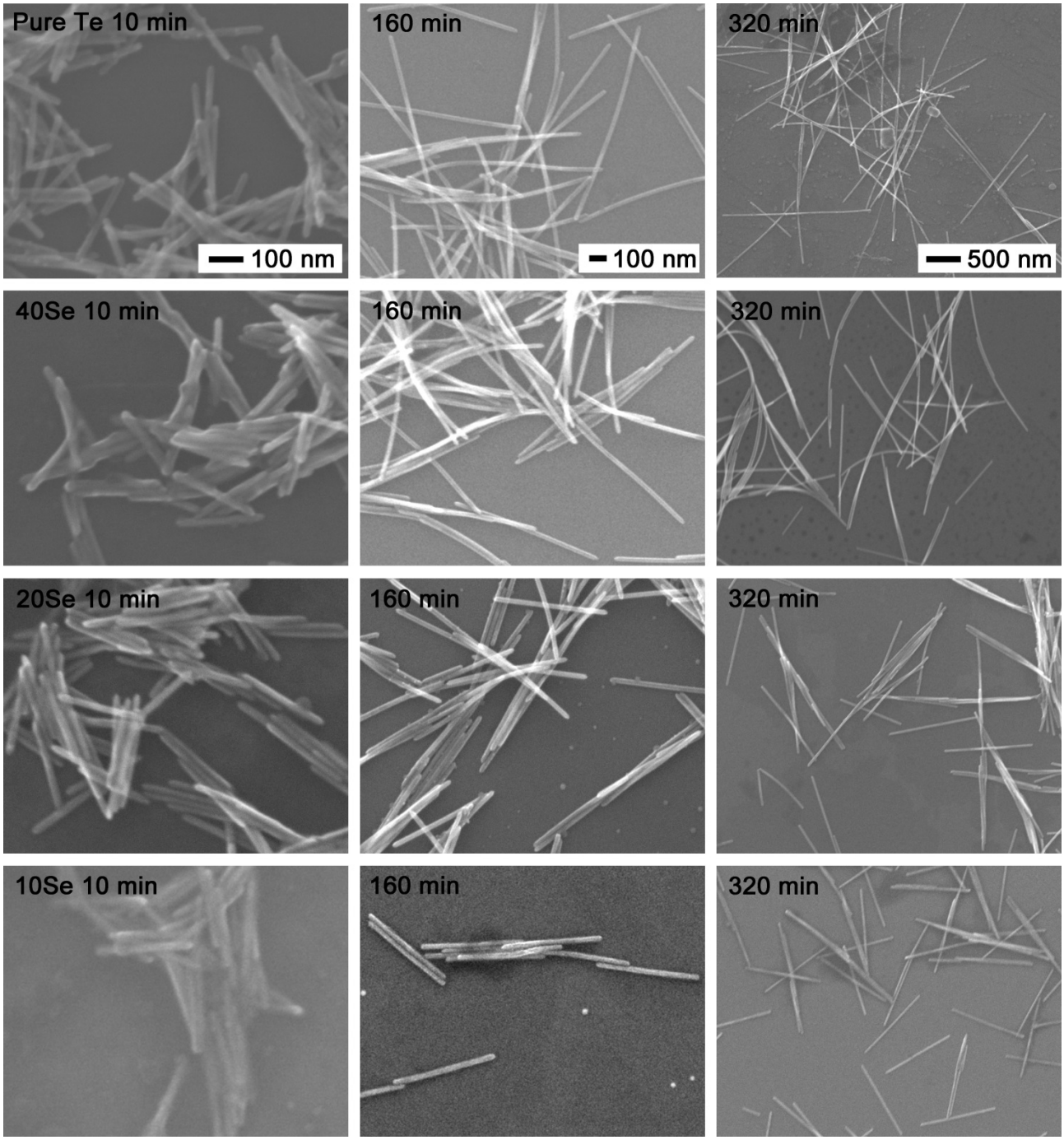

Figure S1. Length profile of nanowires in Figure 2 with respect to different selenium injection point and growth time.

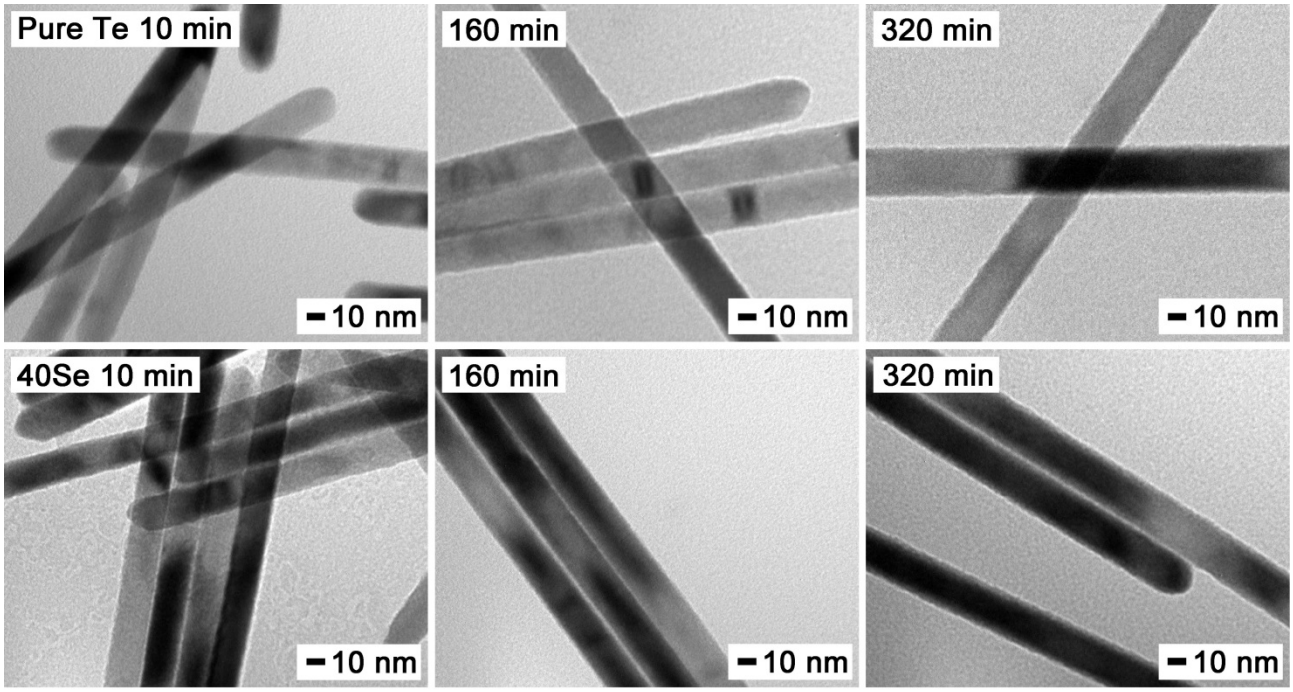

Figure S2. Diameter profile of nanowires in Figure 3 with respect to different selenium injection point and growth time.

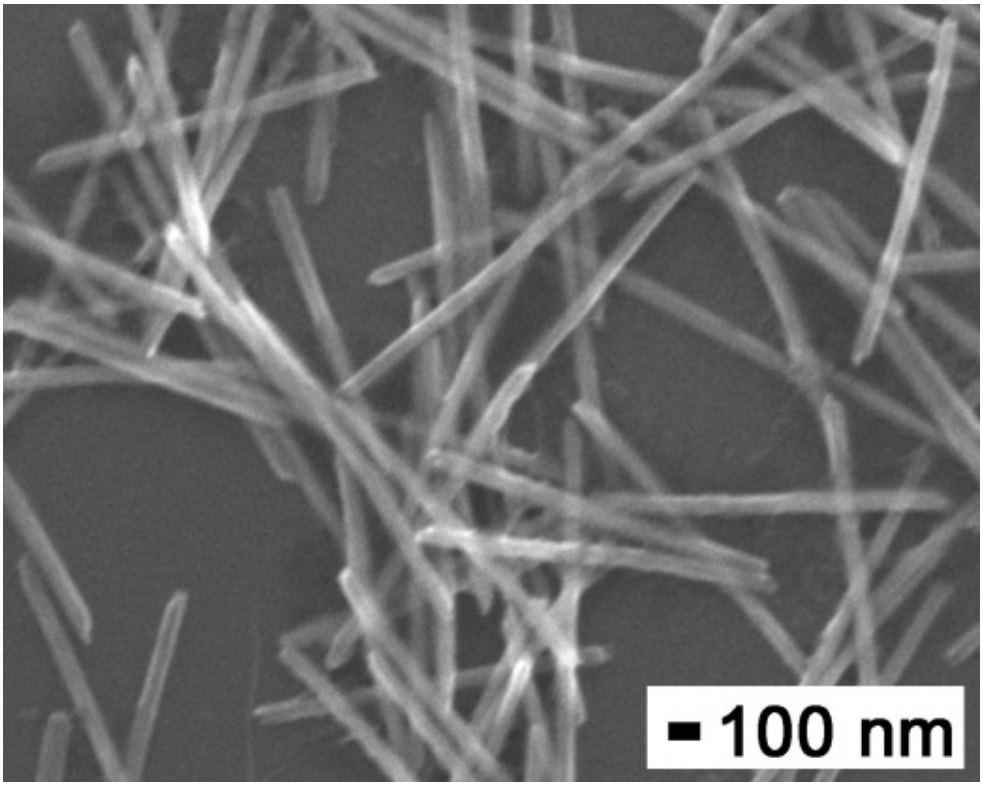

Figure S3. Te nanorods obtained from a supernatant solution of Se-doped Te nanorods. with supernatant of 'Se injection (10 min)' sample. Se was doped after 10 min reaction of the Te nanorods, and the reaction was allowed to proceed for 150 min. The solution was centrifuged and the supernatant solution were transferred into another reaction batch. An excess amount of reductant (5 ml of hydroxyl amine solution, 50 v/v%) was added to the new reaction batch. Temperature was raised to 120 ^{o}C and the reaction was kept for 60 min.

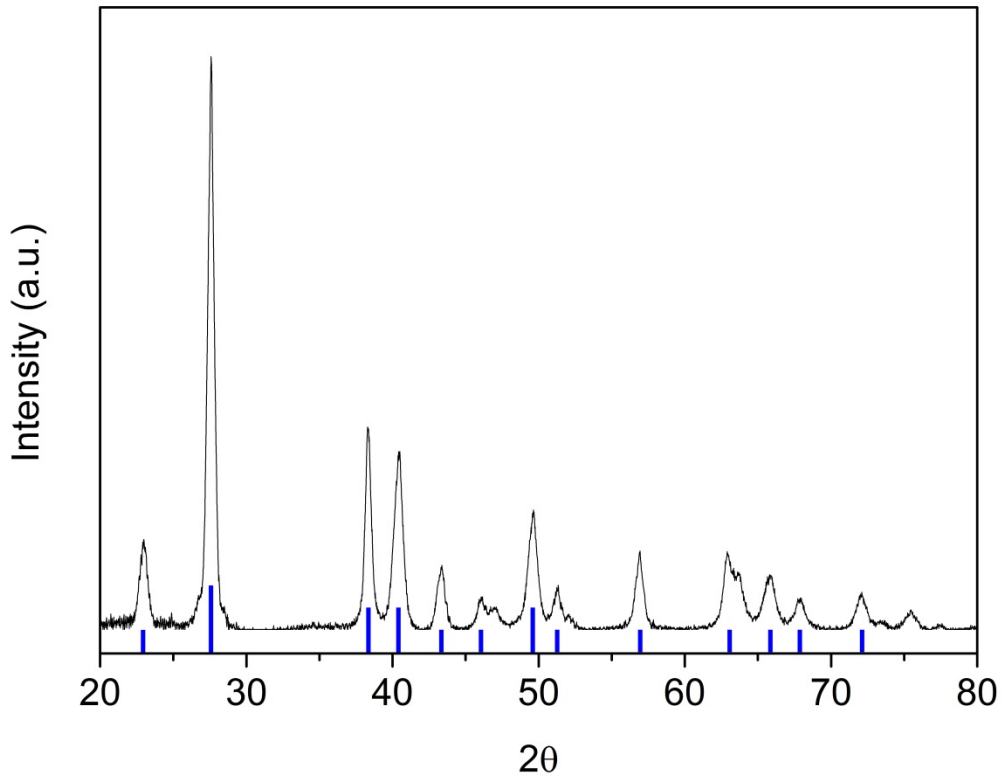

Figure S4. X-ray diffraction result of Te nanorods in Figure 4.

.

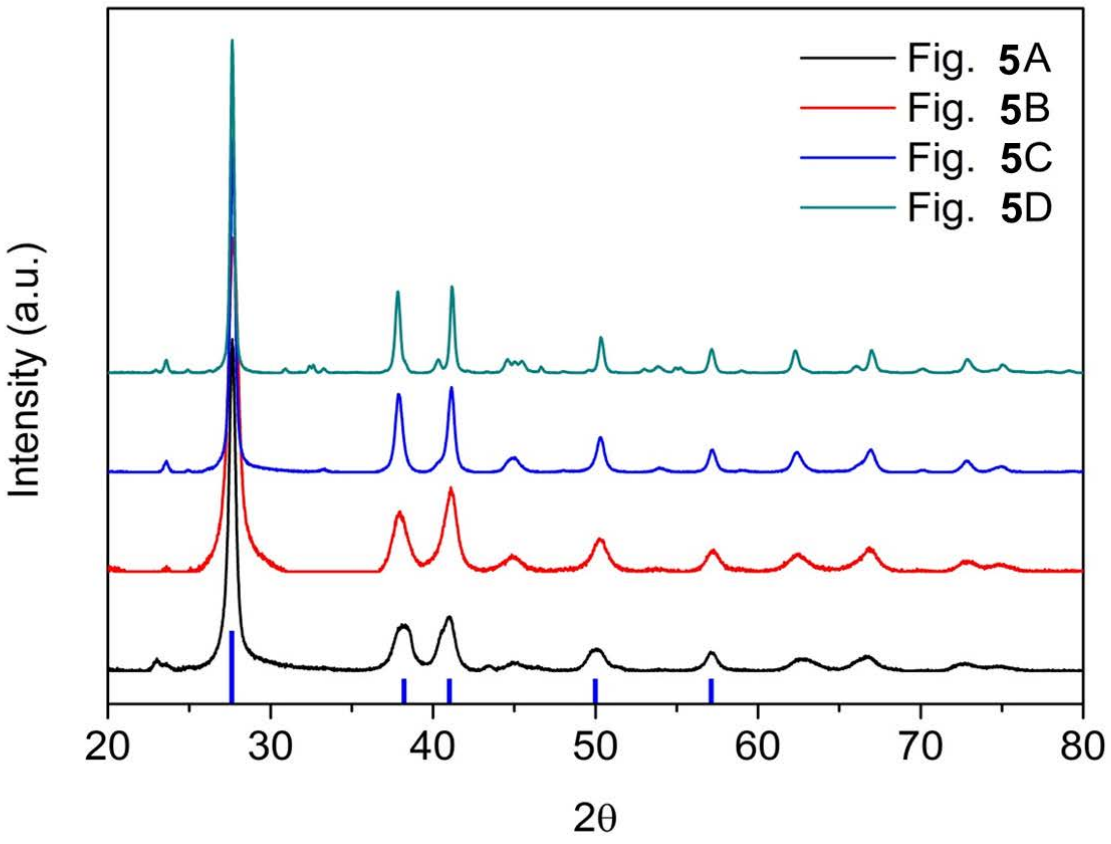

Figure S5. X-ray diffraction result of Bi_2Te_3 nanostructures in Figure 5.

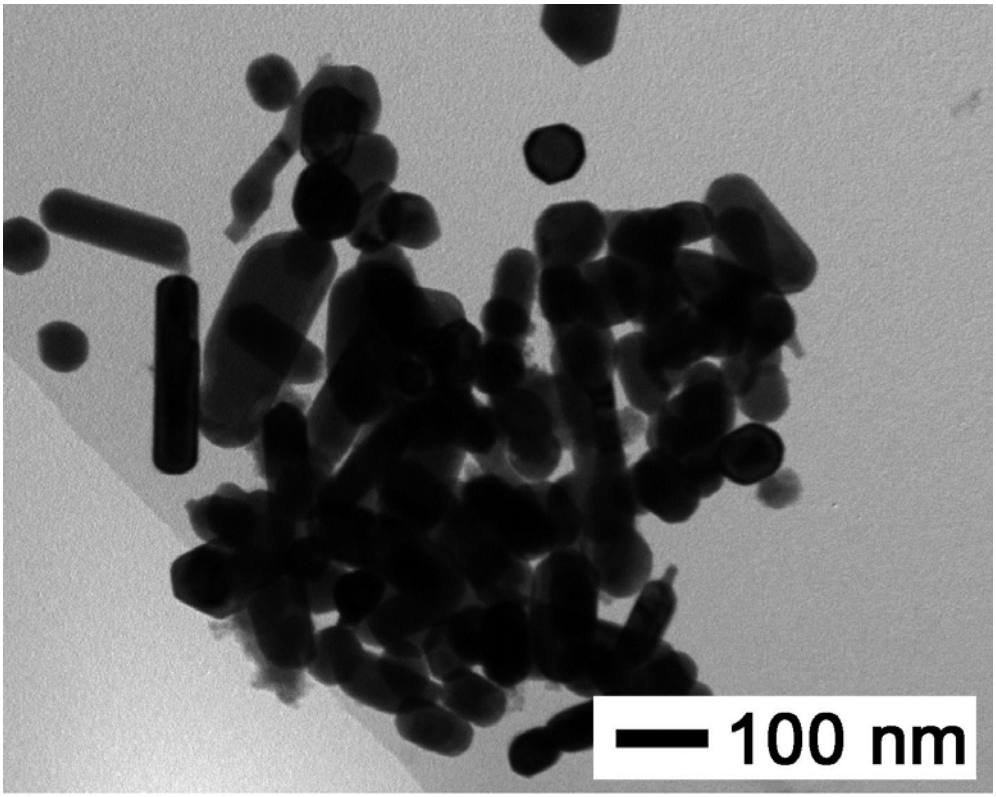

Figure S6. PbTe nanorod transformed from thin, long Te nanorod at 160 ^{o}C.

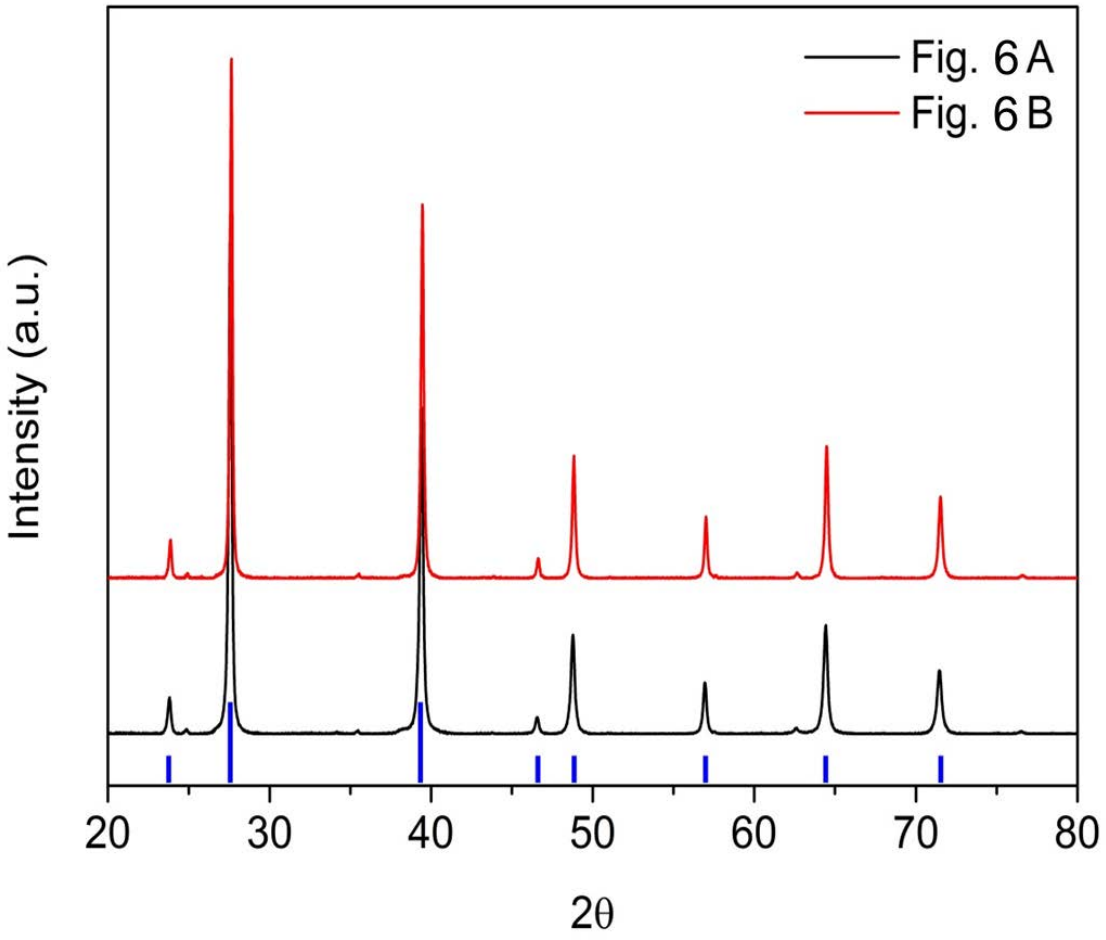

Figure S7. X-ray diffraction result of PbTe nanostructures in Figure 6.

Figure S8. Supernatant solution after reducing the unreacted Te by excessive amount of hydrazine solution. The supernatant solution was collected by centrifuge from a batch for pure Te nanorods which was at 100 ^{o}C for 150 min.